APPENDIX 3

A new instrument to measure the solar aureole from an unstable platform

Joseph M. Ritter and Kenneth J. Voss

Physics Department, University of Miami

Coral Gables, Fl. 33124

305 284 2323 ext 2

fax 305 284 4222

voss@physics.miami.edu

Abstract

A new instrument is described which can measure the sky radiance distribution near the solar disk even when operated on an unstable platform. An imaging detector is used to image the sky around the sun, while an occulter on a long pole blocks out the direct solar radiation. The occulter has a Neutral Density filter in the center which places an image of the solar disk in each image. This allows accurate directional information to be obtained, eliminates possible ambiguities about the angular position of the data, and increases the accuracy of the measurement. A special triggering device aids in making these measurements on a ship. This instrument will be used in field studies of atmospheric aerosols and in satellite validation campaigns.

1. Introduction

Aerosols (solid and liquid particles suspended in the atmosphere) play an important role in determining the Earth's radiation budget (and hence its climate), as well as influencing the chemical composition of the gaseous atmosphere. Aerosols can affect the Earth radiation budget both directly (by scattering and absorbing solar and terrestrial radiation) and indirectly (by modifying cloud properties through their role as cloud condensation nuclei). Unfortunately the global impact of the aerosols optical effects are not well understood. In fact, the uncertainty in the aerosol radiative forcing is larger than

the uncertainty in climate forcing by all greenhouse gases released over the past century (Houghton, et al. 1995). To reduce this uncertainty, improved measurements of the aerosol optical properties are needed for aerosol and climate field studies.

In addition, aerosol optical properties must be understood to interpret satellite observations of the earth's surface since much of the signal received by a satellite is caused by the intervening aerosols. Thus to validate remote satellite measurements of ocean and land properties we need to improve our understanding of the aerosols optical properties.

The solar aureole is the region of enhanced brightness surrounding the sun caused by the scattering of light by aerosols. Radiometric measurements of the solar aureole, when combined with spectral extinction data, can yield data products such as the aerosol size distribution and the aerosol scattering phase function for small scattering angles (Nakajima et al. 1983; Nakajima et al. 1996). For vicarious calibration of ocean color satellite sensors it is desirable to make these measurements at sea (Clark et al. 1997). At sea, platform motion coupled with the large dynamic range of the aureole radiance requires an instrument with a high signal-to-noise ratio, accurate pointing, fast triggering, short exposure times, low jitter, as well as sensor stability.

An imaging radiometer meeting these requirements has been developed and will be described. The imaging nature of the instrument allows measurement of sky radiance within one degree of the center of the solar disk even when deployed on an unstable platform such as a ship.

2. Instrument Description

Previous successful approaches to solar aureole radiometry have involved scanning radiometers on stable platforms (Holben et al. 1996). A new approach was required for shipborne operation where platform motion interferes with the scanning motion. Our approach uses an electronic camera to acquire the circumsolar sky radiance in a single image. Use of a camera ensures accurate direction registration, while modern CCD cameras have the dynamic range necessary for measuring the aureole.

The system components are illustrated in Fig. 1. In brief, the system employs a cooled 512x512 CCD array, 35 mm lens and filter wheel, internal and external cooling system, and sun alignment sensor with associated triggering and digitizing electronics. This package is mounted on a 2m pole and pointed manually toward the sun where an occulter mounted on the end of the pole attenuates the direct sunlight and completely shadows the camera aperture. A sun alignment sensor on the system automatically exposes the CCD when the camera orientation is correct. Instrument control and data acquisition is performed by a remote desktop computer. At this time the instrument components will be described in detail.

a. Occulter

The camera aperture is shadowed by the solar occulter so that scattered radiation entering the aperture is a minimum of 1/2 degree from the instrument optical axis. The solar disk itself subtends a half-angle of 1/4 degree at the instrument. The center of the occulter is a neutral density filter. The attenuated image of the solar disk, when combined with ephemeris data, can be used to determine the azimuth and zenith coordinates corresponding to each CCD pixel.

b. Filter Wheel

After the occulter, the first optical element the light entering the system encounters is the filter wheel housing window. This window is coated with an antireflection coating, and has a 1 cm clear inside diameter. Inside the filter wheel housing, 10 nm interference filters centered at 440, 560, 670, and 860 nm are used to limit the spectral bandpass of the instrument. The filter wheel and housing provides an effective light seal with its neighboring components without significantly extending the optical path. Since this system is only looking at a narrow angular range around the sun, the variation in bandpass of the filters with angular position is negligible (<1%).

Each interference filter is paired with a neutral density filter to optimally utilize the available dynamic range of the sensor. Each spectral channel response is adjusted for near saturation at 1.0 degree from the center of the solar disk with the exception of the 440 nm channel. The low system response at 440 nm would have required longer exposure times to achieve this level and lead to potential blurring effects caused by platform motion.

c. Lens

After passing through the interference and neutral density filters the light enters a camera lens. The current lens system is a standard 35 mm lens with a 50 mm focal length stopped at f/15. With this lens, the instrument has an angular resolution of 0.05 degrees and a field of view of +/- 7.5 degrees centered on the sun.

d. Shutter

An electromechanical shutter is employed in this system. A computer controlled integration and shuttering system ensures low integration time jitter (<10μs) while

exposing rapidly enough (19 msec) to eliminate image blur due to ship motion. The uncertainty in the retrieval of absolute radiance data is directly proportional to the uncertainty in the time the shutter is open from one exposure to the next. Quantitative assessment of jitter, and other calibration issues are addressed in the next section.

e. Pointing and triggering

An essential feature for shipborne applications is a unique sun-sensing trigger device that trips the shutter only when suitable alignment of the sun with the instrument optical axis is achieved. The trigger developed for this instrument consists of a long, baffled collimating tube with a window and neutral density filter at one end, and a photodiode amplifier package at the other. The axis of the tube is aligned parallel to the optical axis of the aureolemeter. When the tube (and thus the aureolemeter) is aligned with the sun, the photodiode is activated and a pulse is generated. The pulse is amplified and shaped, then used to trigger the shutter. This scheme allows measurement of the aureole to within 1 degree of the edge of the solar disk even when deployed on an unstable platform such as a ship.

f. Detector

A commercially available camera (Spectrasource MCD-1000) is used as the image detector. The CCD array used is a 512-by-512 array (TK512). Double correlated sampling digitizes individual pixels at 16 bit resolution. This system provides a signal to noise ratio of 10^3, with dark noise variation less than 11 counts. The array temperature is actively servo-controlled by Peltier cooling. An external cooling system was constructed to help draw additional heat from the instrument, and to ensure sensor stability in field deployments.

g. Data acquisition and control

A Macintosh desktop computer is employed to control data acquisition as well as primary data reduction. Software was written to provide a menu driven user interface, and control image digitization, storage, shuttering as well as perform field diagnostics. Interrupt routines are written in native assembly language to accommodate strict timing requirements. The software incorporates a control loop allowing complete remote system operation by the experimenter, usually located outdoors with the sensor 50 to 100 feet from the control system. Complementary instruments are employed to provide optical depth, measurement location, ambient pressure, humidity and temperature data.

3. Instrument Calibration and Characterization

There are several calibration steps required to convert the camera output into calibrated sky radiance data. In addition, the electro-optical system must be characterized to understand the performance limitations of the system. These steps are now detailed.

a. *Angular Calibration*

Angular calibration is required to determine the mapping between the image location on the array focal plane and the corresponding angle in real space. This was done in two ways. In one test an object was imaged at a known distance. The angular subtence of the object was calculated, and this was used to calibrate the angular field of the image. The result was then verified by placing the instrument on a precision rotary table, imaging a point source, and then acquiring an image. The camera was then rotated by a known angle and another image acquired. This was done for angles from 0 to 7 degrees. The pixel displacement of the light source in the image was then determined and agreed with

the displacement expected from the first test to within 0.05 degrees. Each pixel covers a 0.05 degree wide (full angle) field of view.

b. Dark Signal

There are several components of the dark signal which are not easily separable. An experiment was performed to determine the time dependent thermally generated dark current and its impact on signal to noise degradation. A series of dark images were taken with exposure times ranging from 19 msec to 100 seconds. For each image the average value from 100 pixels in the center of the image was recorded. The slope of the resulting dark signal versus time indicates that approximately 8 thermal counts per second per pixel are generated with the sensor at the nominal sensor operating temperature of 252 Kelvin. The normal exposure time for a sky image is 19 msec, thus these thermal counts become significant only if the CCD is not cleared immediately prior to acquiring an image. Thus we chose to continuously clock out charge from the chip prior to exposing an image. There is also a position dependent dark signal, a result of pixel-to-pixel bias variations as well as local well fabrication differences. Immediately following each sky image a dark image is acquired. The dark image is then subtracted off of the sky data image as the first step in the data processing. In addition to this dark noise, readout noise from the sampling electronics occurs and is difficult to independently estimate or separate from the dark noise. All of the noise factors together result in a standard deviation per pixel of 11 counts.

c. Linearity Characterization

Charge coupled device arrays are inherently linear devices when properly biased. Nevertheless, an experiment was performed to determine the overall system response

linearity. The camera imaged a diffusing plaque from a constant distance. The source illuminating the diffuser was then placed at logarithmically spaced distances for each set of exposures in order to achieve the desired plaque irradiances. An image data set was acquired at each step and an average value from the center 100 pixels was recorded. The results are shown in Fig. 2. The linearity of output signal relative to input light was verified for 3 orders of magnitude of viewed radiance.

d. Absolute Radiometric Flux Calibration

In order to determine the absolute spectral response of each CCD pixel, it was necessary to first determine the absolute transmission curve $T(\lambda)$ for each interference - neutral density filter pair. A monochromator (Optronics 740A) configured for 1 nm resolution was used to measure the filter transmission. The measurement extended to where the transmission was 10^{-4} of the peak transmittance on each side of the filter's peak. This was repeated for all 4 interference filters. The interference filters' bandwidth and center frequencies are summarized in Table 1. .

Following this the system was set to view a nearly lambertian calibrated Spectralon plaque at 45 degrees off normal. The plaque was illuminated by a 1000 W standard lamp (FEL, spectral irradiance calibration traceable to NIST). This provided a known source of radiance for the system. Unfortunately, this laboratory source is much dimmer than the solar aureole, thus we could not include the neutral density filters in this measurement. The transmission of the neutral density filters were determined in the same manner as the interference filters, and these transmission values were folded into the calibration. An absolute calibration factor was then determined for each pixel, and a matrix was constructed such that when applied pixel-by-pixel to image data, after the

dark signal removal, it corrects both for optical rolloff as well as generating absolute radiance values.

e. Absolute Radiometric Accuracy and Precision

Tests were performed to quantify absolute radiometric jitter, i.e. repeatability or the lack thereof between measurements. A plaque was illuminated with a steady source and then 20 images were acquired. After applying the above calibration procedure to each image, a 100 pixel sample near the center of each image was selected for analysis. The results show that the absolute jitter, i.e. radiometric precision, for the entire electromechanical system is on the order of 0.1%. The absolute calibration of the system is limited by the accuracy of the standard lamp and is assumed to be on the order of 3%.

f. Optical Beam Spread Function

Since the lens is focussed to infinity, for a perfect lens, all photons incident at one angle are mapped to exactly 1 point on the array. To test our system a helium-neon laser beam was expanded to a diameter larger than the camera aperture in order to both fill the aperture and to decrease the divergence of the laser beam. This beam then directly illuminated the camera aperture from a series of angles (0, 1, 2, 3, 4, 5, 6 and 7 degrees). At each angle an image was acquired. These measurements showed that over 90% of the counts were contained within 0.1 degrees from the center of the spot.

4. Data Acquisition and Reduction

During the data acquisition sequence, upon alignment with the sun, the instrument digitizes and stores a sky radiance image, a dark image, and housekeeping data.

To reduce the data, a series of automated programs were written in Spyglass Transform. These routines act on a collection of raw data (image and dark) files to remove the dark signal. The resulting images are processed to produce image arrays where pixel values are calibrated radiance, and pixel positions correspond to small solid

angle elements of the sky at each point in the instrument's field of view. Following this procedure, the user then decides by visual inspection which images merit further analysis. This step is necessary to filter for cloud contamination or measurement artifacts (field of view obstruction, flaring, etc.). The next step in the analysis is completed by a series of automated image analysis programs developed for the Matlab data analysis package.

The Matlab programs opens a data file containing the calibrated image. Embedded in this file are coordinates of the pixel closest to the center of the sun, while a separate data file contains solar air mass, the channel wavelength mapping, solar constants, Rayleigh, aerosol and ozone optical depths for the dataset. The image header is stripped and the data transposed and stored in a format suitable for further analysis. A similarly dimensioned (512x512) matrix is generated where each pixel value corresponds to the air mass at the corresponding camera image pixel. Finally a matrix is constructed where each pixel value is the scattering angle at the corresponding data image pixel. An example radiance image is shown in Figure 3.

Due to diffraction effects it is necessary to filter or "digitally occult" some pixels near the image center. The software determines the points which lie within a small user-definable angle of the sun center and generates a mask to zero data in the original radiance image array. These occulted pixels are shown as the white circle in Fig. 3. This mask is also applied to the scattering angle and air mass matrices.

It is useful to examine the images for sky homogeneity by examining left / right symmetry of radiance vs. scattering angle. A typical scatter plot, for a good data set, showing this symmetry is shown in Fig. 4. After determining symmetry, it is necessary to resample the flagged almucantar data into appropriately sized solid angle bins. This is

accomplished by setting a user-definable (half-cone angle) bin size (usually 0.25 degrees) and averaging over all data within that scattering cone, within the appropriate air mass limits and where the data has not been digitally occulted. The almucantar sampled is shown as the white band in Fig. 3 . An example plot showing the resampled almucantor radiance for the solar aureole is shown in Fig. 5. Once this aureole radiance is determined it can be combined with independent measurements of the aerosol optical depth to determine the small angle scattering phase function, and a parameter related to the slope of the large particle size distribution.

As an example derived product, Fig. 6 illustrates several aerosol phase functions derived from the aureole measurements (Ritter 1998). These are derived from several measurements of the solar aureole performed on a single day. They were derived assuming single scattering and that the aerosols were contained in a single layer in the atmosphere. They show a small variation in the small angle portion of the aerosol scattering function over this period.

5. Conclusions

A new instrument has been described which can measure the sky radiance distribution near the solar disk even when operated on an unstable platform. Use of an imaging detector, and the presence of an image of the solar disk in each image, allow accurate directional information to be obtained. This eliminates possible ambiguities about the angular position of the data, and increases the accuracy of the measurement. A special

triggering device aids in making these measurements on a ship. This instrument will be used in field studies of atmospheric aerosols and in satellite validation campaigns.

6. Acknowledgements

The authors are grateful for support from the NASA Goddard Space Flight Center under contracts NAS5-31363. We would also like to thank Mr. Albert Chapin for his help in machining the instrument.

References

Clark, D. K., H. R. Gordon, K. J. Voss, Y. Ge, W. Broenkow, and C. Trees, 1997: Validation of atmospheric correction over the oceans. J. Geophys. Res., **102**, 17209 - 17217.

Holben, B., A. Setzer, T. F. Eck, A. Pereira and I. Slutsker, 1996: Effect of Dry-Season Biomass Burning on Amazon Basin Aerosol Concentrations and Optical Properties. J. Geophys. Res., **101**, 1992-1994.

Houghton, J. T., L. G. Meira Filho, B. A. Callendar, N. Harris, A. Kattenberg and K. Maskell (Editors), 1996: *Intergovernmental Panel on Climate Change (IPCC), Climate Change (1995): the Science of Climate Change*, Cambridge University Press, N.Y.

Nakajima, T., M. Tanaka and T. Yamauchi,1983: Retrieval of the Optical Properties of Aerosols from Aureole and Extinction Data. Appl. Opt., **22**, 2951-2959.

Nakajima, T., G. Tonna, R. Rao, P. Boi, Y.J. Kaufman and B. Holben, 1996: Use of Sky Brightness Measurements from Ground for Remote Sensing of Particulate Polydispersions, Appl. Opt., 35, 2672-2686.

Ritter, J. M., 1998: Remote measurement of aerosol scattering properties and the development of a novel imaging solar aureole radiometer, Ph.D. Thesis, University of Miami, Coral Gables, Fl. 33124.

Figure Captions

1) Schematic of aureole camera system.

2) Linearity plot obtained with aureole camera system. Data points are 10 x 10 pixel averages in the center of the image. System shows good linearity at over 3 orders of magnitude. Standard deviation of the pixel values are displayed as error bars in the x direction.

3) Sample aureole image contour. Several important features in the image are identified.

4) Plot of the aureole, separating left and right sides of the aureole almucantor. This illustrates the symmetry of the data set. This type of plot can be used for quality control of the data.

5) Sampled aureole almucantor data.

6) Aerosol phase function derived from aureole data. Phase functions were derived using single scattering and assuming the aerosols were contained in a single layer.

Filter (nm)	Centroid (nm)	Full width at half maximum (nm)
440	440.9	10
560	561.3	10
670	670.2	12
860	856.6	13

Table1. Interference filter bandwidth and center frequencies

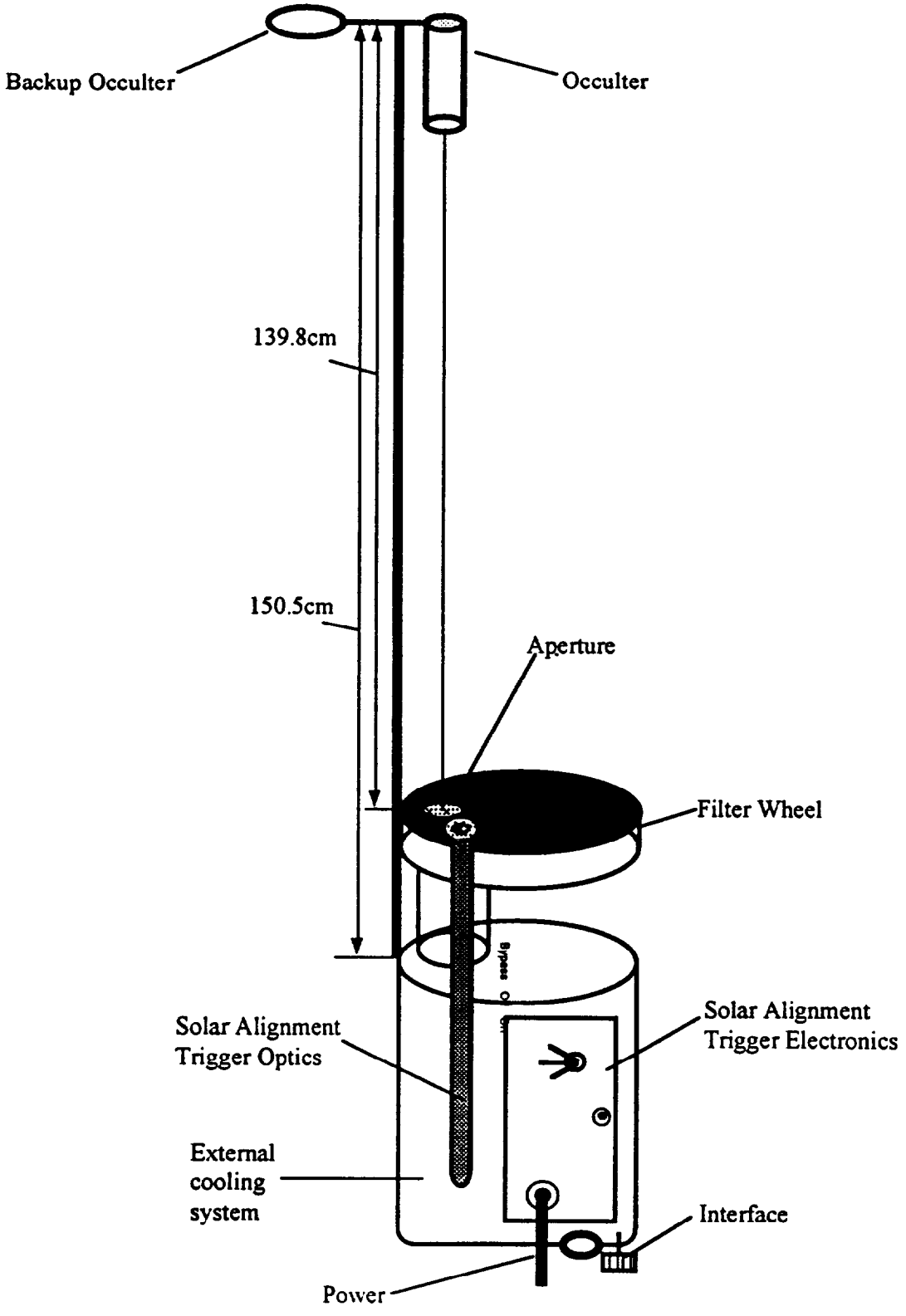
Backup Occulter
Occulter
139.8cm
150.5cm
Aperture
Filter Wheel
Solar Alignment
Trigger Optics
Solar Alignment
Trigger Electronics
External
cooling
system
Interface
Power

Fig 1

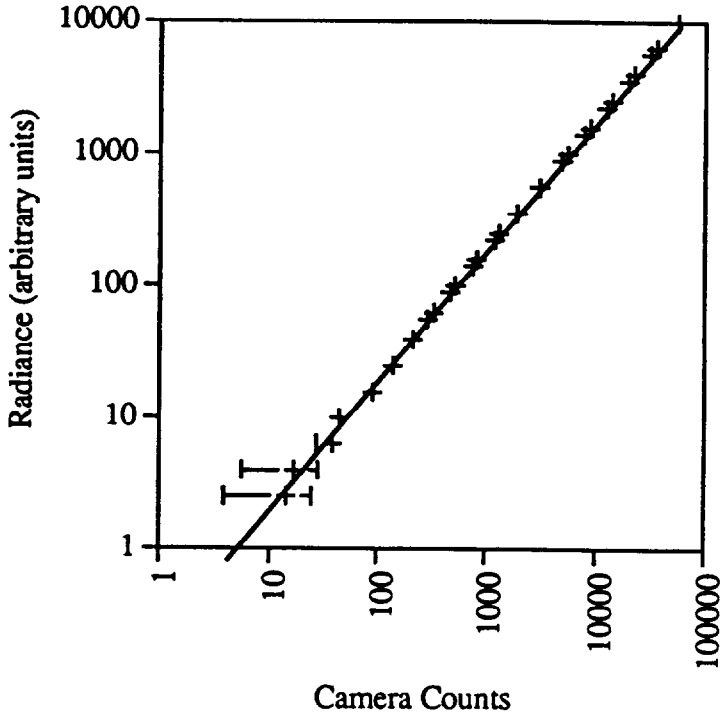
10000
1000
100
10
1
Radiance (arbitrary units)
1
10
100
1000
10000
100000
Camera Counts

Fig 2

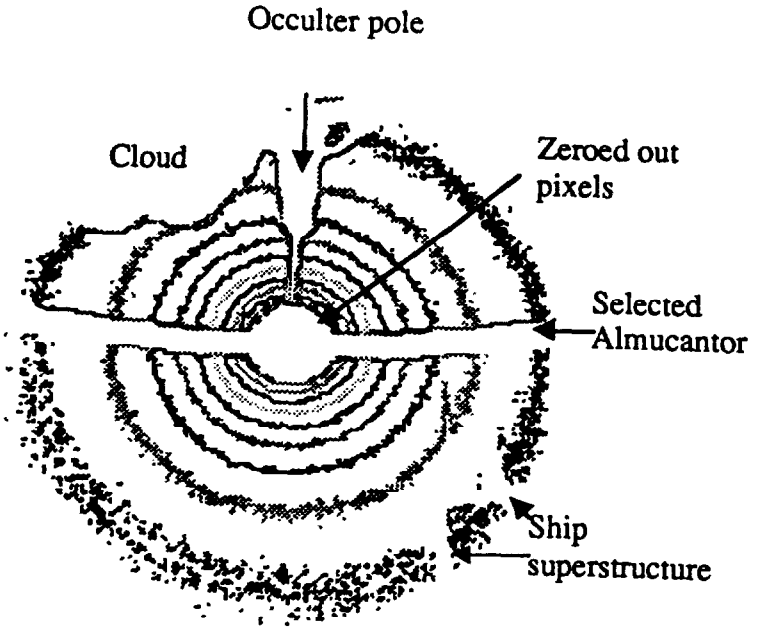
Occulter pole
Cloud
Zeroed out pixels
Selected Almucantor
Ship superstructure

Fig 3

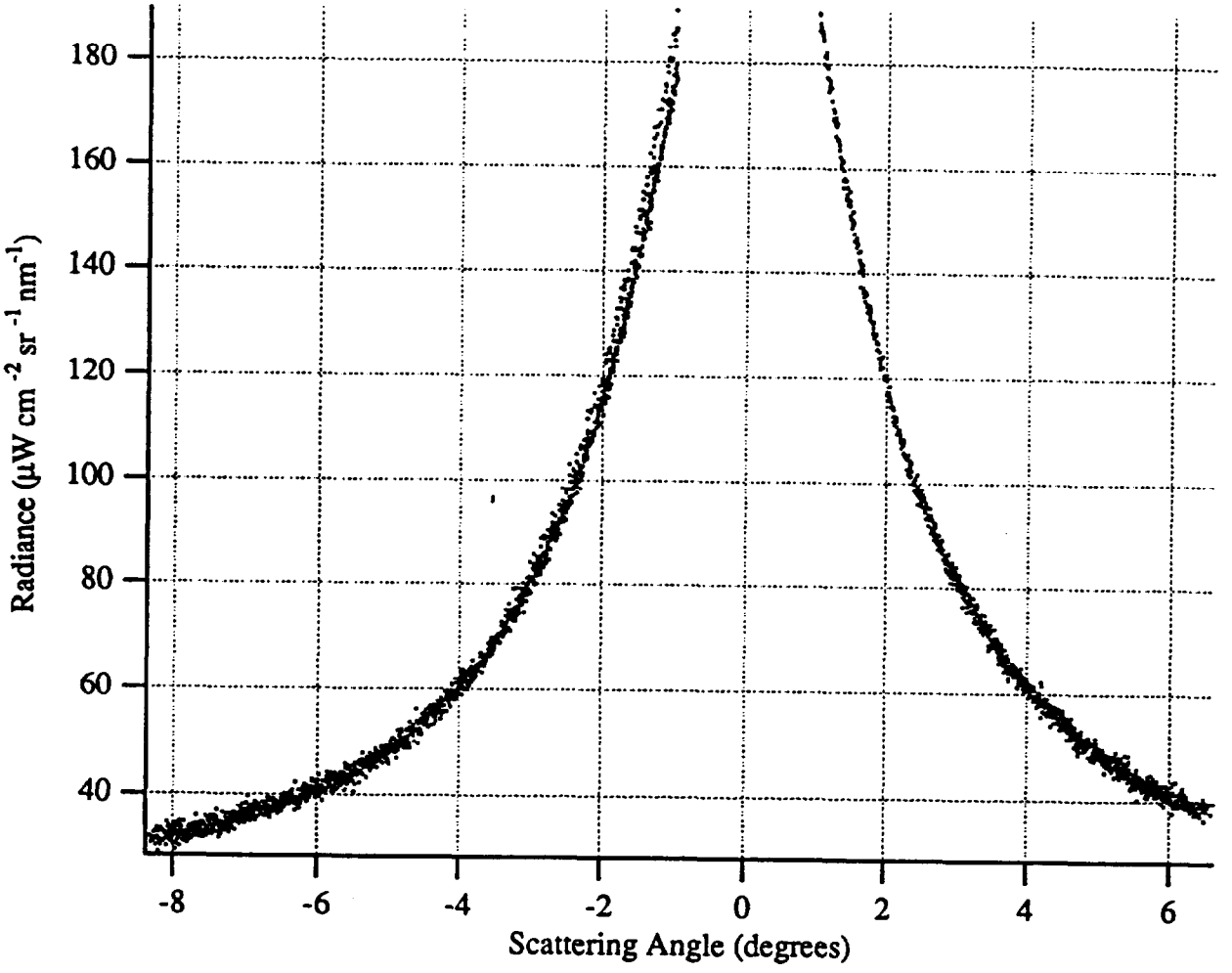
180
160
140
120
100
80
60
40
Radiance (μW cm -2 sr -1 nm-1)
-8
-6
-4
-2
0
2
4
6
Scattering Angle (degrees)

Fig 4

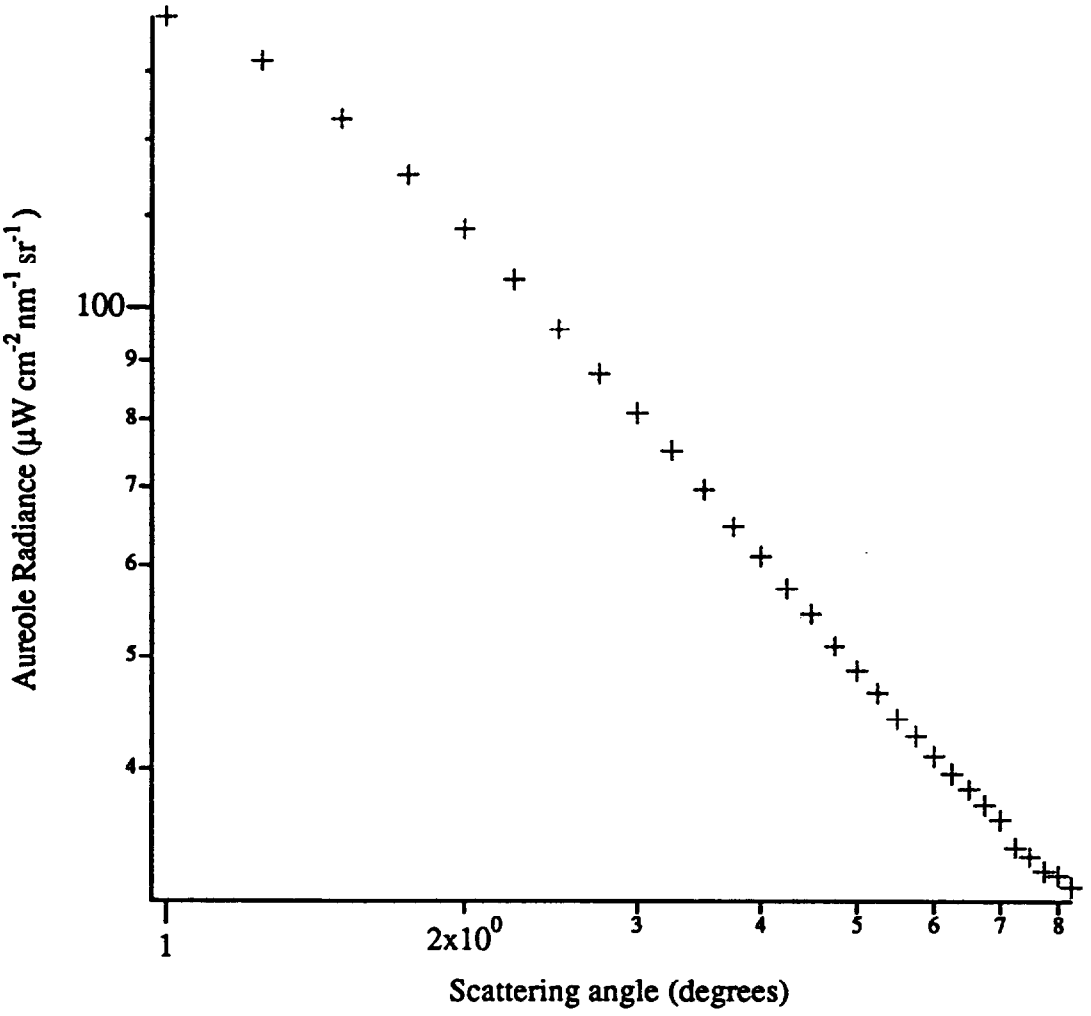
Aureole Radiance (μW cm-2 nm-1 sr-1)
100
9
8
7
6
5
4
1
2x10^0
3
4
5
6
7
8
Scattering angle (degrees)

Fig 5

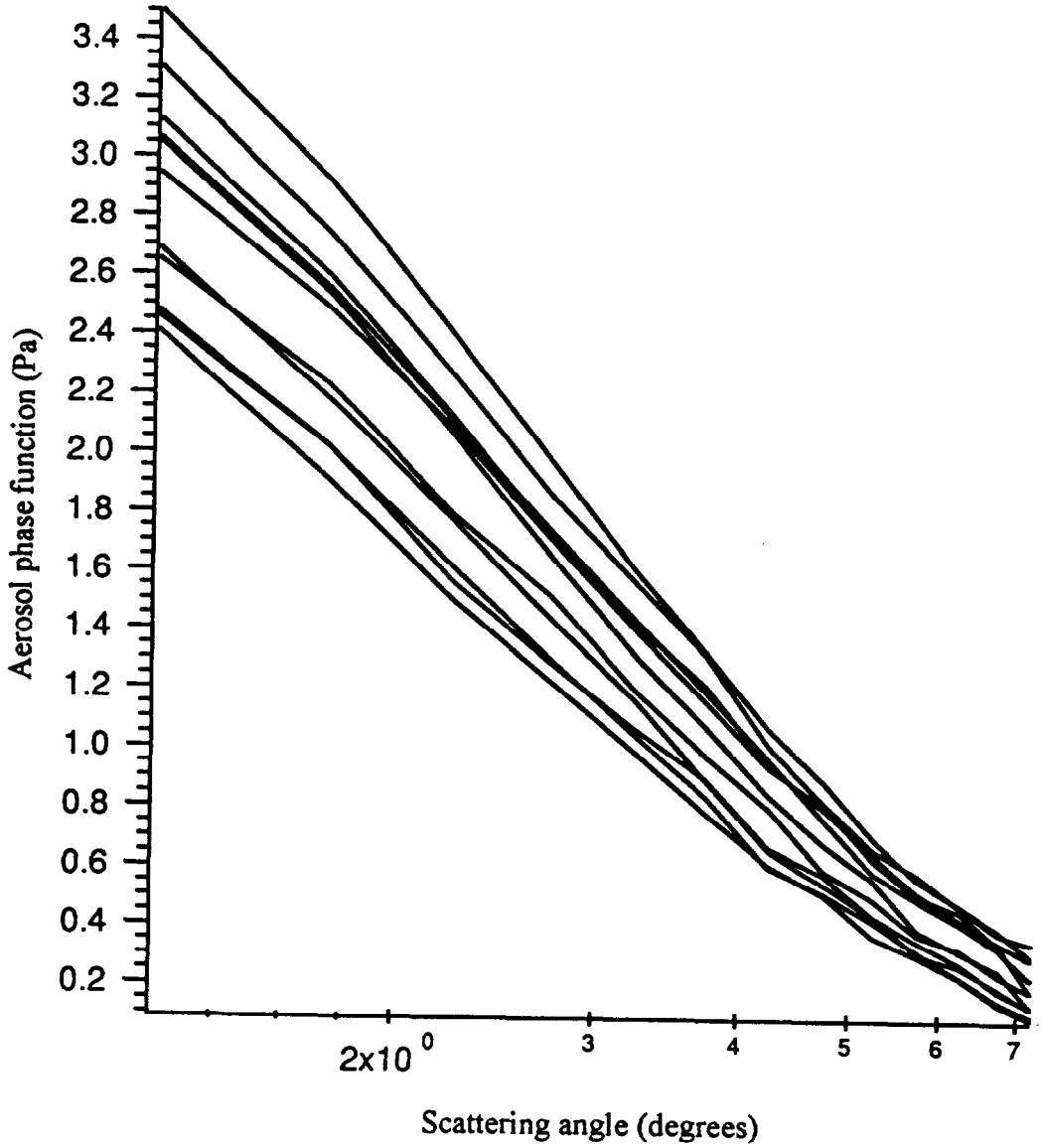
Aerosol phase function (Pa)
3.4
3.2
3.0
2.8
2.6
2.4
2.2
2.0
1.8
1.6
1.4
1.2
1.0
0.8
0.6
0.4
0.2
2x10 0
3
4
5
6
7
Scattering angle (degrees)

Fig 6